Elastocapillary interaction for particles trapped at the isotropic-nematic liquid crystal interface

J.-C. Loudet*

Université de Bordeaux, CNRS, Centre de Recherche Paul Pascal (UMR 5031), 33600 Pessac, France

(Received 17 January 2024; accepted 11 April 2024; published 9 May 2024)

We present numerical simulations on pairwise interactions between particles trapped at an isotropic-nematic liquid crystal (Iso-N) interface. The particles are subject to elastocapillary interactions arising from interfacial deformations and elastic distortions of the nematic phase. We use a recent model based on a phase-field approach [see Qiu *et al.*, Phys. Rev. E **103**, 022706 (2021)] to take into account the coupling between elastic and capillary phenomena. The pair potential is computed in a two-dimensional geometry for a range of particle separations and two anchoring configurations. The first configuration leads to the presence of an anchoring conflict at the three-phase contact line, whereas such a conflict does not exist for the second one. In the first case, the results show that significant interfacial deformations and downward particle displacements occur, resulting in sizable attractive capillary interactions able to overcome repulsive elastic forces at intermediate separations. The pair potential exhibits an equilibrium distance since elastic repulsions prevail at short range and prevent the clustering of particles. However, in the absence of any anchoring conflict, the interfacial deformations are very small and the capillary forces have a negligible contribution to the pair potential, which is fully repulsive and overwhelmed by elastic forces. These results suggest that the self-assembly properties of particles floating at Iso-N interfaces might be controlled by tuning anchoring conflicts.

DOI: 10.1103/PhysRevE.109.054603

I. INTRODUCTION

It is well established that particles trapped at fluid interfaces may undergo a specific interaction known as capillary interaction [1–3]. These interactions originate from the overlap of interfacial deformations that may occur in the vicinity of the floating particles due to, e.g., their buoyant weight, their shape, or the presence of electrical charges at their surface [3–9]. They have been extensively investigated at isotropic fluid interfaces such as air- or oil-water interfaces and employed to control the self-assembly of particles with sizes ranging from a few tens of nanometers up to a few millimeters [6–9].

However, less known is the behavior of particles attached to complex fluid interfaces such as, e.g., air- or water-liquid crystal (LC) interfaces. Because LCs are partially ordered media, and therefore, bear elastic properties [10], the physical properties of such systems are expected to be mainly governed by the interplay of capillary and elastic phenomena. In fact, particles at LC interfaces may be viewed as the merging of two research areas, which have been very thoroughly explored, but in a rather independent way so far. On the one hand, we have the aforementioned capillary interactions at isotropic fluid interfaces and, on the other hand, we have the "LC colloids," which consist of colloidal particles immersed in a bulk LC matrix, mostly in the nematic (N) phase [11]. In the latter case, the self-assembly of particles is governed by elastic interactions driven by deformations of the director field surrounding the inclusions. Depending on the anchoring conditions of LC molecules at the particle surface, topological defects may nucleate as well and play an essential role [11–19].

However, so far, only a handful of studies have attempted to bridge the gap between these two research lines by considering particles attached to isotropic (Iso)-LC interfaces. Little is known on how capillary and elastic interactions will combine to rule the assembly of a collection of objects. On their own, capillary and elastic interactions can be either attractive or repulsive, long-ranged (power-law behavior), anisotropic in nature (e.g., of dipolar or quadrupolar symmetry), and feature energies way above the thermal energy [8,9,11]. But what are the characteristics (e.g., range intensity, symmetry) of pairwise elastocapillary interactions for instance? Most of the existing works, mainly experimental, focused only on a few special cases, often in confined geometries (e.g., thin nematic films, nematic shells), either at the single particle level [20–23], or involving a large collection of microparticles. For example, in the latter case, two-dimensional (2D) crystal-like structures and chain-like clusters were observed at the air-nematic LC (NLC) [24–28] and water-NLC interfaces [29,30]. The first study dealing with pairwise interactions is due to Gharbi *et al.* [27], who used optical tweezers to manipulate solid microbeads spread at the free surface of nematic films. They reported the existence of an *unstable* equilibrium distance $r_c \approx 5R$, where R is the bead radius, beyond which the particles repelled elastically, and below which they irreversibly aggregated due to supposed topological defect reorganizations. However, both the nematic director field and interfacial profile around the beads could not be characterized precisely. Afterwards, only two more experimental investigations followed up on the subject, at least with nematic LCs. The work of Liu *et al.* [31] examined the influence of particle shape on elastocapillary interactions by depositing microcylinders at the free surface of a thin nematic film. It was found that the particle assembly was largely dominated

*jean-christophe.loudet@u-bordeaux.fr

by capillary attractions, whereas elastic effects controlled the orientation of the resulting aggregates. Within the same group, Wei *et al.* [32] probed the vibrational phonon modes of 2D crystalline packings of microspheres at the air-NLC interface and attempted to relate the spring constant of the particle network to their interactions. Unfortunately, no definite conclusion could be drawn due to a limited range in particle separation.

Besides nematic LCs, Gharbi *et al.* [33] also investigated elastocapillary interactions between micrometer-sized solid beads attached to free-standing smectic films. Using polarized optical microscopy combined with video tracking tools, these authors reported attractive elastocapillary interactions arising from distortions of the smectic free surface and bulk deformations of the smectic layers. The physical picture is more complicated here because of the presence of focal conics domains and edge dislocations in the meniscus around the inclusions.

Despite the above discoveries, there is still a lack of theoretical understanding of the observed phenomena, even for simple objects such as microspheres, and the modeling studies that appeared on the subject are scarce. Andrienko *et al.* [34,35] performed the first numerical simulations of particles attached to an Iso-N interface, but no interfacial forces nor three-phase contact line (CL) were taken into account in their analysis. In order to rationalize the early observations of Ref. [24], Oettel *et al.* [36] derived approximate analytical calculations pertaining to the long-range character of pairwise interactions. In this case, a repulsive interaction was predicted both from capillary and elastic effects, provided that the thickness of the nematic film is much larger than the particle size. Besides the aforementioned investigations, we are not aware of any other detailed theoretical or numerical reports on these topics.

Recently, our group developed a model, based on a phase-field (PF) method, capable of describing elastocapillary flows of LCs [37,38]. In Ref. [39], we adapted this model in numerical simulations to probe the behavior of a single particle trapped at an Iso-N interface. The results showed that potentially large interfacial deformations and particle displacements, both on the order of $0.5R$, may take place as a result of the coupling between elastic, capillary (surface tension), and anchoring effects. Since the nematic director field is also distorted in the vicinity of the particle, such a configuration may serve as a good starting point to gain more insight on pairwise elastocapillary interactions. As far as we know, no predictions exist so far for these interactions at intermediate and short ranges, i.e., when the separation distance is less than a few particle radii.

In this paper, we extend our previous work by considering a pair of particles placed at the Iso-N interface and study their interaction as a function of the separation distance. Using the model designed in Refs. [37,38], we carry out 2D numerical simulations to first derive qualitative physical trends prior to considering more sophisticated three-dimensional computations. Our intention is to shed some light on a novel type of colloidal interactions that clearly lacks in-depth characterizations, as revealed from the above literature survey. In particular, we wish to elucidate the relative importance of capillary and elastic interactions by tuning the system parameters.

The paper is organized as follows. The model is briefly presented in Sec. II. It is numerically solved using a finite-element method in a 2D geometry. In Sec. III, we study the pair interaction between particles attached to an Iso-N interface for a range of separations and two anchoring conditions of LC molecules at the particles surface and at the fluid interface. When an anchoring conflict exists at the CL, it is shown that a small, but non-negligible, capillary attraction can contribute to the interaction potential in addition to an elastic repulsion which is always dominant at short range. We discuss our results in light of existing works before concluding in Sec. IV.

II. THEORETICAL MODEL AND NUMERICAL METHOD

As in Ref. [39], we have used the model of Qiu *et al.* [37,38] to address the pair interaction of particles floating at the Iso-N interface. This model has two key features that make it possible to study the coupling between elastic and capillary phenomena: (i) a tensor order parameter $\mathbb{Q}$ able to account for the LC microstructure including potential topological defects and (ii) a PF formalism that accurately represents the Iso-N interfacial tension and the nematic anchoring stress by approximating a sharp-interface limit. All the details and validation examples of the model have been reported elsewhere [37,38]. In the following, we will only summarize the main ideas and give the governing equations.

A. Governing equations

In the PF-based model of Qiu *et al.* [37,38], the Iso-N interface is treated as having a small but finite thickness across which the PF variable, ϕ, and all physical properties of the system, change continuously. ϕ takes distinct values in each phase. In our case, the N phase (respectively, Iso phase) corresponds to $\phi = -1$ (respectively, $\phi = 1$) and the interface location may be defined by the contour level $\phi = 0$. The two phases mix in the thin diffuse interfacial region and the profile of ϕ is determined by a mixing free energy consisting of two competing terms, one that promotes complete mixing of the phases and the other that favors total phase separation [40,41]. In the so-called sharp-interface limit, the mixing energy gives rise to an isotropic surface tension given by $\sigma = 2\sqrt{2}\lambda/3\epsilon$, where λ [N] is the mixing energy density and ϵ [m] is the capillary width representative of the interfacial thickness [40,41].

The energy-based formulation of the PF method allows easy incorporation of the properties of the N phase, which admits a natural energetic description. In our model, the bulk elastic distortions and topological defects in the N phase are described by the phenomenological, $\mathbb{Q}$-based Landau-de Gennes free energy, whereas a diffuse interface variant of the well-known Rapini-Papoular anchoring energy accounts for the finite-strength anchoring of LC molecules at the Iso-N interface. The expressions of all free energies are omitted here but can be found in Ref. [38]. Note that we assume an infinitely strong anchoring of LC molecules on the solid particle and, consequently, the anchoring energy at the N-solid interface is not considered.

The governing equations are (i) the Cahn-Hilliard equation for the transport of the phase-field ϕ [40,41], (ii) an

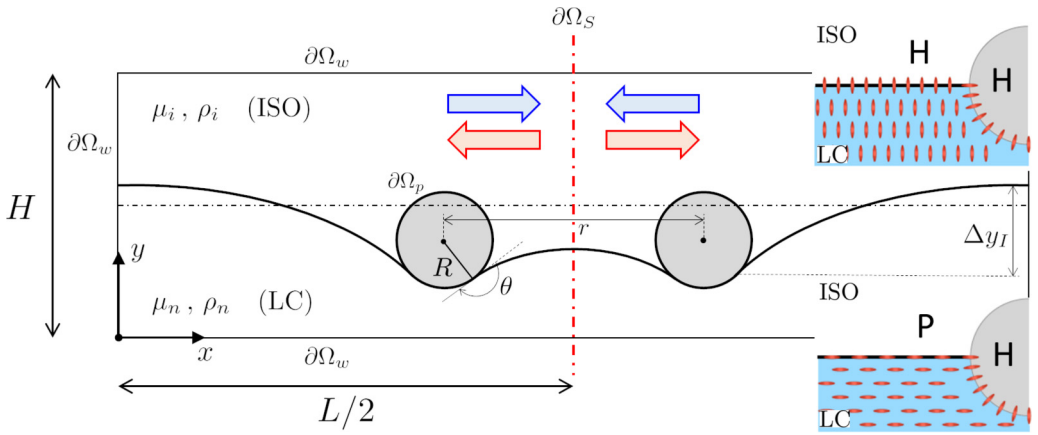

FIG. 1. Sketch of the simulation domain. Box size: $(H, L) = (16R, 28R)$. Symbols: θ , contact angle; Δy_I , interfacial deformation; $\partial\Omega_p$, particle surface; $\partial\Omega_w$, box wall; $\partial\Omega_S$, symmetry plane (see text for other symbols definitions). The blue and red arrows indicate that the particles may interact either attractively, repulsively, or both. Insets: Initial bulk and anchoring conditions of the order parameter $\mathbb{Q}$. The small ellipsoids symbolize the LC molecules (not to scale). A homeotropic (H) or planar (P) anchoring is prescribed at the Iso-N interface, while a homeotropic condition is imposed at the particle surface.

evolution equation for $\mathbb{Q}$ derived from the Beris-Edwards (BE) theory [42,43], and (iii) the continuity and momentum equations of the two-phase system assuming incompressible fluids:

$$\frac{\partial\phi}{\partial t} + \mathbf{v}\cdot\boldsymbol{\nabla}\phi = \gamma\lambda\nabla^2[-\nabla^2\phi + \phi(\phi^2-1)/\epsilon^2], \tag{1}$$

$$\frac{\partial\mathbb{Q}}{\partial t} + \mathbf{v}\cdot\boldsymbol{\nabla}\mathbb{Q} = \mathbb{S} + \Gamma\mathbb{H}, \tag{2}$$

$$\boldsymbol{\nabla}\cdot\mathbf{v} = 0, \tag{3}$$

$$\rho(\phi)\left(\frac{\partial\mathbf{v}}{\partial t} + \mathbf{v}\cdot\boldsymbol{\nabla}\mathbf{v}\right) = \boldsymbol{\nabla}\cdot\mathbb{T} + \mu\boldsymbol{\nabla}\phi\,, \tag{4}$$

where $\mathbf{v}$ is the fluid velocity. In Eq. (1), γ (m^3 s/kg) is the (constant) mobility of the diffuse interface. In Eq. (2), Γ (Pa^{-1} s^{-1}) is the (constant) collective rotational diffusion coefficient of the N phase, $\mathbb{H}(\phi, \mathbb{Q}, \boldsymbol{\nabla}\phi, \boldsymbol{\nabla}\mathbb{Q})$ is the molecular field tensor, and $\mathbb{S}(\boldsymbol{\nabla}\mathbf{v}, \mathbb{Q})$ is the corotation tensor [43]. Both tensors have been altered in our PF method to take into account the anchoring conditions (either homeotropic or planar) at the Iso-N interface. The detailed expressions can be found in Ref. [38]. The last body-force term in Eq. (4) ($\mu\boldsymbol{\nabla}\phi$) is the diffuse-interface equivalent of the interfacial tension [40,44], where μ is the chemical potential defined from the PF mixing free energy [38]. The density $\rho(\phi) = \frac{1+\phi}{2}\rho_i + \frac{1-\phi}{2}\rho_n$ is an average between the two components, where the subscript i (respectively, n) refers to the isotropic (respectively, nematic) phase. The total stress tensor $\mathbb{T}$ can be written in the following form:

$$\mathbb{T} = -p\mathbb{I} + (1+\phi)\eta_i\mathbb{D} + (1-\phi)\eta_n\mathbb{D} + \mathbb{T}_n\,, \tag{5}$$

where p is the pressure and $\mathbb{D} = [(\boldsymbol{\nabla}\mathbf{v})^\intercal + \boldsymbol{\nabla}\mathbf{v}]/2$ is the rate of deformation tensor. The second term is the viscous stress from the isotropic phase while the third term is a viscous stress of the nematic phase with a constant effective viscosity η_n , i.e., independent of the molecular orientation [42,43]. The last term ($\mathbb{T}_n$) in Eq. (5) is the nematic stress tensor, whose expression has been generalized from the bulk BE theory to take into account the anchoring constraints on the moving Iso-N interface [38]. Equations (1)–(4) must be supplemented by initial and boundary conditions (BCs), which will be specified below in Sec. II C.

In addition to the above fluid equations, we also need to take into account the equations of motion of the interacting particles attached to the Iso-N interface. As explained in Sec. II C, only the vertical displacement (y direction) of the particles will be allowed in the present simulations. Ignoring gravity (Sec. II C), the particle translational velocity (U_y) is governed by $M\dot{U}_y = F_y$, with the initial condition $U_y|_{t=0} = 0$, the dot meaning differentiation with respect to time. M is the particle mass and F_y is the total force exerted on the particle along the y direction. F_y consists of viscous, elastic, and capillary forces and can be computed from the following contour integral:

$$F_y = \hat{\mathbf{y}}\cdot\oint_{\partial\Omega_p}(\mathbb{T} + \mathbb{T}_c)\cdot\hat{\mathbf{m}}\,ds, \tag{6}$$

where $\hat{\mathbf{y}}$ is the unit normal vector along the y axis, $\partial\Omega_p$ is the particle contour (cf. Fig. 1), $\hat{\mathbf{m}}$ is the outward unit normal vector to $\partial\Omega_p$, and $\mathbb{T}$ is the stress tensor defined in Eq. (5). Note that the total force exerted on the particle along the x direction, F_x , can be computed in a similar manner (Sec. III). In Eq. (6), $\mathbb{T}_c$ is the capillary stress tensor given in Ref. [41]: $\mathbb{T}_c = f_{\mathrm{mix}}\,\mathbb{I} - \lambda\boldsymbol{\nabla}\phi\boldsymbol{\nabla}\phi$, where f_{mix} is the PF mixing free energy [40,41]. Once U_y has been determined, the vertical position of the particle (y_p) can be updated by solving $\dot{y}_p = U_y$.

B. Numerical method

As in our previous work [39], we use the finite-element computational software COMSOL MULTIPHYSICS [45] to solve numerically the governing equations, and their associated boundary conditions, together with the particle's equations of motion. Details of the numerical approximation and validation examples can be found in Refs. [37,38]. To resolve the vertical motion of the particle, we employ the built-in moving mesh module of COMSOL based on an Ar-

bitrary Lagrangian-Eulerian scheme. The amplitude of this motion is always moderate, i.e., typically $\lesssim 0.5R$, and does not incur any remeshing event. We design nonuniform triangular meshes fitted with subdomains whose mesh size is adjusted to ensure a sufficient resolution of both the fluid interface [41,44,46,47] and the topological defects that may nucleate and migrate in the course of simulations [39]. Outside of the subdomains, the mesh size is coarser to save computational time.

C. Geometry and parameters

In this section, we specify the parameters and the geometry employed in our 2D simulations (Fig. 1). Two solid particles of radius R, separated by a center-to-center distance r, are trapped at the interface between a Newtonian isotropic fluid and a nematic LC. The whole system is confined in a box of length $L = 28R$ and height $H = 16R$. However, because of symmetry, only half of the box may be considered and the actual simulated domain has dimensions $(H, L/2)$. We find that this box size is a reasonable trade-off between reduced box size effects and "acceptable" computational times, i.e., not exceeding 1 or 2 days for a single run. Indeed, since the fluid interface has to be finely resolved (see below), the longer the box, the more time consuming the computations.

A homeotropic (H) anchoring condition is prescribed at the particle surface, while either a homeotropic or planar (P) anchoring is imposed at the Iso-N interface (see insets in Fig. 1). These BCs result in two anchoring configurations that will be referred to as the H-H and P-H configurations hereafter, respectively. Notice that, in the former situation, an anchoring conflict exists at the CL, whereas such a conflict is absent in the latter one. Two other anchoring configurations, i.e., the P-P and H-P setups, exist as well but they have been disregarded here for they are expected to play a similar role than the H-H and P-H geometries in terms of the anchoring conflict, respectively.

The anchoring strength W [48] is tunable at the Iso-N interface, while only a rigid anchoring is set on the particle wall, as aforesaid. For the initial condition, we require the far-field LC molecules to be oriented along the vertical (respectively, horizontal) direction in the H-H (respectively, P-H) configuration with an equilibrium scalar order parameter $q_e = 0.81$ (Table I) [38]. For the CH equation [Eq. (1)], and as in our previous work [39], no-flux BCs were prescribed across all solid boundaries ($\partial\Omega_{w,p}$): $\hat{\mathbf{m}} \cdot \boldsymbol{\nabla}\mu|_{\partial\Omega_{w,p}} = 0$, where $\hat{\mathbf{m}}$ is the outward unit normal vector to a given boundary. Next, the equilibrium value of the contact angle, θ, is enforced on the particle surface at the CL, and only $\theta = 90^\circ$ will be considered here. The particle's center of mass is allowed to move vertically and the Iso-N interface is initially flat. We also impose a 90° contact angle on $\partial\Omega_w$ (left side) and $\partial\Omega_S$ (Fig. 1), meaning that the interface is kept flat there but it is free to move up or down. Indeed, we will see later that the interface is likely to be deformed and displaced from its initial position because of the interplay of elastic, surface tension, and anchoring effects.

For the continuity and momentum equations [Eqs. (3) and (4)], the particle surface is a nonslip wall, whereas on boundaries that mimic infinity or on $\partial\Omega_S$, we use either no penetration or free slip conditions. Note that PF-based models can naturally handle the CL dynamics thanks to intrinsic diffusive processes [46,47,49–51]. Furthermore, as in Ref. [39], we are typically simulating the behavior of micrometer-sized particles floating at the Iso-N interface. In this case, it is well established that the interfacial deformations arising from the particle's buoyant weight are negligible and can be safely discarded (see, e.g., Ref. [3]). Thus, gravity is ignored in the present simulations.

The pair interaction potential is computed in a static manner for a range of r values. Specifically, for a given r, the particles are allowed to equilibrate in the vertical direction until the whole system reaches a steady state. The interaction force, defined (in norm) as $F_{\text{int}} = 2F_x$, where F_x is the total force acting on the (left) particle in the x direction, is then computed prior to setting a new r and starting another simulation. We use a sign convention such that the particles repel (respectively, attract) one another if F_{int} is positive (respectively, negative).

Unless otherwise stated, our simulations are run with the base parameters listed in Appendix A. When presenting the results, we use dimensionless variables marked by an asterisk, which will be defined as they come along in the text.

III. RESULTS AND DISCUSSION

A. H-H configuration

We first present the results on the interaction of two nearby floating particles at the Iso-N interface in the H-H configuration (Fig. 1). As aforesaid, the H-H configuration is characterized by an anchoring conflict at the CL, which makes it suitable to study the interplay of elastic and capillary phenomena in particle interactions since both the order parameter field and the interface are distorted. As explained in Sec. II C, the particles are initially placed at a given center-to-center distance r and the Iso-N interface is flat at time $t = 0$. The particles are free to move up or down, depending on the forces acting on them. In turn, the shape of the fluid interface is likely to be altered by the particle motion. For all r, we only consider the case $\theta = 90^\circ$ for which the anchoring conflict is the strongest at the CL.

Figure 2 shows typical steady-state contour plots of Q_{22}^2 (grayscale) computed for $r^* = r/2R = 6.2$ [Fig. 2(a)] and $r^* = 2$ [Fig. 2(b)]. A close-up view of Fig. 2(b) near the particle is displayed in Fig. 2(c). The isotropic phase displays as black ($\mathbb{Q} = 0$), whereas in the nematic phase, bright areas (large values of Q_{22}^2) correspond to LC molecules pointing upwards, which is the bulk initial condition for $\mathbb{Q}$ (Sec. II C). On the other hand, dark regions (small values of Q_{22}^2) indicate $\mathbb{Q}$-field distortions and we see that, in Fig. 2(a), they are symmetrically located on either side of the lower part of the particle. Furthermore, close to the CL, a thorough inspection of the director field reveals the formation of tiny topological defects located in the immediate vicinity of the particle surface [Fig. 2(d)]. This texture is consistent with the imposed BCs on $\mathbb{Q}$ at the interface and at the particle surface (Sec. II C). Note that, in three dimensions, the elastic distortions surrounding the particle in Fig. 2(a) would have a quadrupolar symmetry, and thus, from an elastic viewpoint,

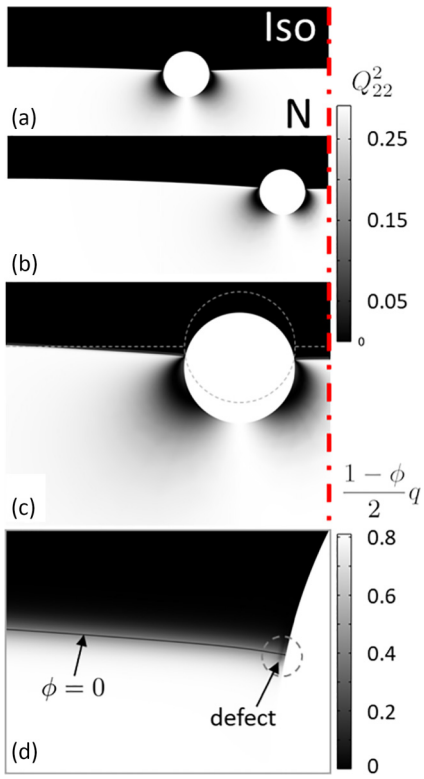

FIG. 2. H-H configuration. [(a)–(c)] Contour plots of Q_{22}^2 (grayscale) at steady state. (a) $r^* = r/2R = 6.2$ and (b) $r^* = 2$. The red dot-dashed line to the right indicates the symmetry plane. The full width of the simulation box is displayed in (a) and (b), but only a part of the domain is shown in the vertical direction. (c) Zoomed-in view of (b) near the particle. The gray dashed line and circle represent the initial positions of the interface and the particle, respectively. (d) Blown-up view of (c) near the contact line. The grayscale shows the concentration-weighted scalar order parameter $\frac{1-\phi}{2}q$, with $q_e = 0.81$ (Table I). The tiny dark blurry area located inside the dashed circle signals a topological defect. The curve $\phi = 0$ marks the fluid interface. $\theta = 90°$.

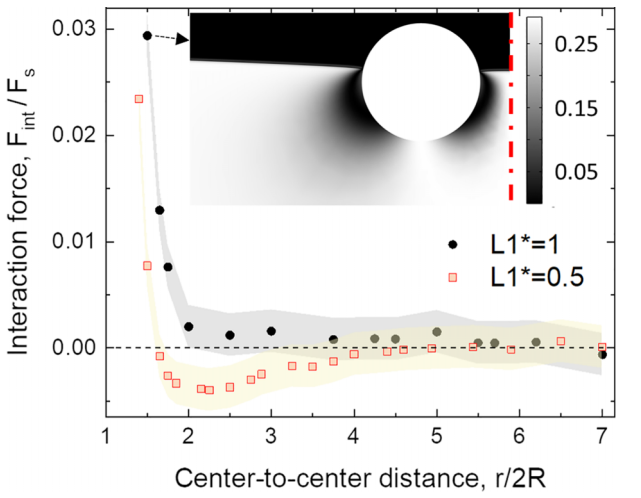

FIG. 3. H-H configuration. Interaction force ($F_{\text{int}}^* = F_{\text{int}}/F_s$) as a function of the center-to-center distance ($r^* = r/2R$) for two values of the elastic constant ($L_1^* = L_1/F_s$). The shaded areas around the data points represent the typical uncertainty interval in the simulations (see text for details). A small attractive well develops at intermediate range ($r^* < 3$) for $L_1^* = 0.5$, whereas an all-repulsive force is computed for $L_1^* = 1$. Inset: Snapshot obtained for $L_1^* = 1$ and $r^* = 1.5$. The red dot-dashed line symbolizes the symmetry plane. Grayscale: Q_{22}^2. $\theta = 90°$.

such a particle would be expected to behave as an elastic quadrupole [11].

In Fig. 2(a), both interfacial deformations and particle displacement have occurred with respect to the initial state. If we define the interfacial deformation $\Delta y_I = y_w - y_{\text{CL}}$ as the difference between the y location of the interface at the bounding wall (y_w) and that at the CL (y_{CL}) (Fig. 1), then we find $\Delta y_I^* = \Delta y_I/R \simeq 0.16$ and a particle displacement $y_p^* = y_p/R \simeq -0.24$ for the data of Fig. 2(a). As shown in Ref. [39], these results can be rationalized by the presence of an anchoring conflict at the CL, which drives the response of the system in terms of particle motion and interfacial distortion. In Fig. 2(a), the values of Δy_I^* and y_p^* do not differ much from those computed for a single particle at the Iso-N interface for the same parameter set and box size. This is not too surprising since the particles are several radii away from one another and hardly interact or only weakly so.

However, bringing the particles closer at $r^* = 2$ leads to more enhanced interfacial deformations and particle displacement, as revealed in Fig. 2(b). The departure from the initial state is best visualized in the zoomed-in view of Fig. 2(c). Here $\Delta y_I^* \simeq 0.41$ and $y_p^* \simeq -0.4$, i.e., the perturbations amount to a significant fraction of the particle radius. At short range, the particle sinks more into the nematic phase, and in the narrow space between the particles, the interface profile is almost flat due to the strong overlap of interfacial deformations. These features are typical of capillary interactions (see, e.g., Ref. [52]) and indicate that the particles actually undergo a capillary attraction [53]. Note that, because of their negligible buoyant weight (Sec. II C), the particles under consideration would not produce any interfacial deformations if adsorbed at isotropic fluid interfaces. Thus, the occurrence of interfacial distortions and particle motions are specific to the Iso-N interface and arise from the coupling of elastic, capillary, and anchoring effects [39].

As for the nematic field, we may notice a slight left-right asymmetry of the two dark lobes surrounding the particle [Fig. 2(c)]. From the symmetry of these distortions, we rather expect an elastic repulsion of the particles at close range (see below).

To know whether the particles tend to attract or repel one another due to the interplay of elastic, capillary, and anchoring effects, we have computed the interaction force, $F_{\text{int}}^* = F_{\text{int}}/F_s$, exerted on the particle, as explained in Secs. II A and II C, for a range of r and two values of the elastic constant $L_1^* = L_1/F_s$. F_s is an arbitrary force scale derived from characteristic pressure (10^5 Pa) and length (10 nm) scales. It is similar to that used, e.g., in Ref. [54]. The resulting data are compiled in Fig. 3. Note that, for each data point, we carried out several simulations by slightly varying the size of the subdomains that were finely meshed to resolve the Iso-N interface (Sec. II B), including the contact line region. The results showed that the computed force values featured an averaged

uncertainty of about $\pm 1.8 \times 10^{-3}$, which is represented by the shaded areas around the data points.

Next, we focus on the results obtained for $L_1^* = 1$. In this case, we see that the interaction force remains always positive and is therefore repulsive, according to our convention. Hence, despite sizable interfacial deformations ($\Delta y_I^* \simeq 0.1$–0.3), which trigger attractive capillary interactions, the particles tend to stay apart. Furthermore, the closer the particles, the stronger the repulsion, as is evidenced by the sharp increase of the force for $r^* < 2$. This repulsion has an elastic origin, as anticipated, and it can be directly visualized from the asymmetry of the distorted director field around the particle (see inset in Fig. 3): close to contact, the right dark lobe appears less extended and more "compressed" towards the particle surface than its left counterpart. Extrapolating to 3D, our results would be consistent with the fact that elastic quadrupoles repel each other when approaching head-on [55–57].

A similar conclusion holds at short range ($r^* = 1.5$) for the data presented with $L_1^* = 0.5$ since the interaction force is also repulsive (Fig. 3). However, a striking difference is that the force becomes negative for intermediate separations up to $r^* \approx 3.5$ before nearing zero at larger distances. In this region, the dipping of the force is larger than the aforementioned uncertainty interval on the force calculation. Hence, the particles should attract one another for $r^* \lesssim 3$ until an elastically dominant repulsion takes over at short range. Incidentally, this result implies the existence of an equilibrium distance between the particles located at the minimum of the well, here at $r^* \simeq 2$.

Of course, it is natural to think that the aforementioned attraction is of capillary origin and that changing the value of the elastic constant L_1 must have altered the intensity of both the elastic and capillary parts of the interaction. Actually, the idea of tuning L_1 in Fig. 3 was guided by a simple scaling argument derived in Ref. [39], which is based on the competition between the bulk elastic energy and surface energies (surface tension and anchoring). This argument predicts that $\Delta y_I \sim L_1^{-1/2}$, and therefore, decreasing the value of L_1 should enhance interfacial deformations, which, in turn, should boost the intensity of attractive capillary interactions. The numerical data exhibited on Fig. 4 agree with this prediction. On these plots, we have reported the interfacial deformations Δy_I^* [Fig. 4(a)], the particle displacement y_p^* [Fig. 4(b)], and the capillary interaction force $F_{\rm cap}^* = F_{\rm cap}/F_s$ [Fig. 4(c)], taken here to be positive for convenience) as a function of r for the two L_1^* values. In Fig. 4(a), it is clear that the interfacial deformations are larger for $L_1^* = 0.5$ than those recorded for $L_1^* = 1$, and the closer the particles, the more important the difference between the two values. Furthermore, the inset plot in Fig. 4(a) shows that $\Delta y_I(L_1^* = 0.5) \simeq \sqrt{2}\,\Delta y_I(L_1^* = 1)$, i.e., the aforementioned scaling relation ($\Delta y_I \sim L_1^{-1/2}$) is actually quantitatively verified in a satisfying manner. Correlatively, the particle sinks more into the nematic phase for $L_1^* = 0.5$ than for $L_1^* = 1$, i.e., the particle displacement y_p is more negative in the former case than in the latter, as illustrated in Fig. 4(b). This phenomenon would be consistent with the fact that decreasing L_1^* softens the nematic matrix, which allows a deeper immersion of the particle. Finally, the

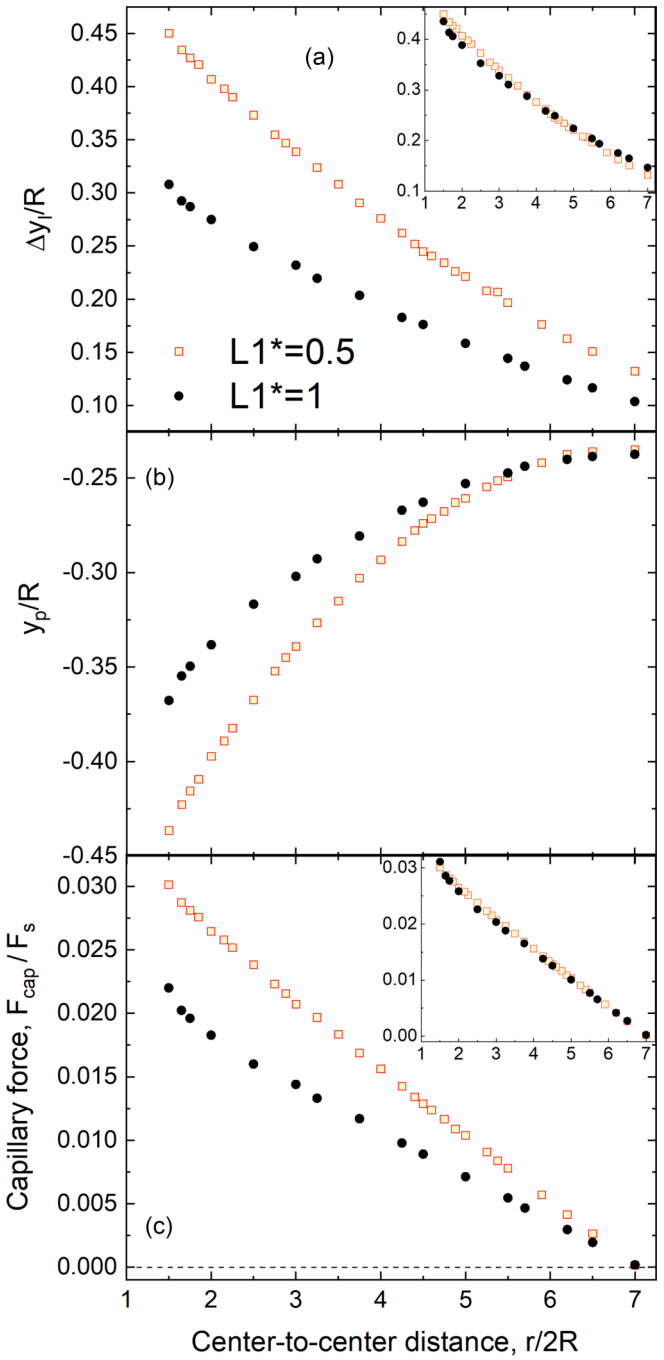

FIG. 4. H-H configuration. Interfacial deformation Δy_I (a), particle displacement y_p (b), and capillary interaction force $F_{\rm cap}$ (c) as a function of the center-to-center distance r for two values of the elastic constant L_1^*. Insets in (a) and (c): verification of the scaling relations $\Delta y_I \sim L_1^{-1/2}$ and $F_{\rm cap} \sim L_1^{-1/2}$, respectively (see text for details).

plot in Fig. 4(c) reveals that the capillary interaction force is enhanced for the smaller L_1^* value, which is expected since $F_{\rm cap} \propto \Delta y_I$ (see Fig. 6 in Appendix B). Incidentally, we also have $F_{\rm cap} \sim L_1^{-1/2}$, as shown in the inset of Fig. 4(c), where it is seen that $F_{\rm cap}(L_1^* = 0.5) \simeq \sqrt{2}\,F_{\rm cap}(L_1^* = 1)$.

In light of the above findings, we may reasonably surmise that the appearance of the attractive well in Fig. 3 for $L_1^* = 0.5$ originates from an enhanced capillary attraction driven by

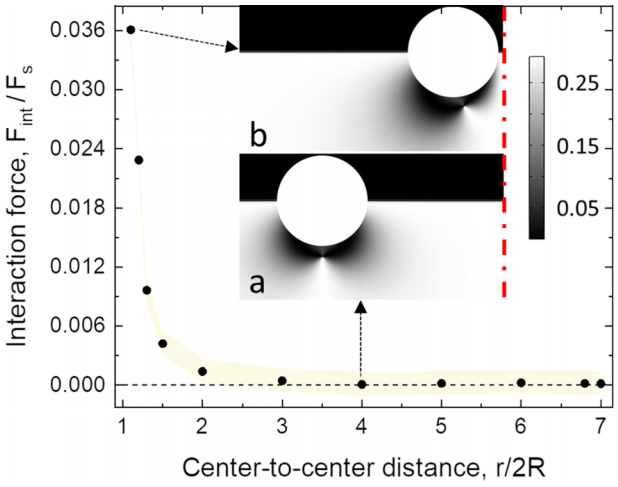

FIG. 5. P-H configuration. Interaction force ($F^*_{\rm int} = F_{\rm int}/F_s$) as a function of the center-to-center distance ($r^* = r/2R$). The interaction potential is repulsive for all separations. As in Fig. 3, the shaded areas around the data points represent the typical uncertainty interval in the simulations (see text for details). Insets: Snapshots obtained for $r^* = 4$ (a) and $r^* = 1.1$ (b). The topological defect located underneath the particle is slightly shifted towards the symmetry plane at very close range (b). The interfacial deformations and particle displacement are negligible here. The red dot-dashed lines symbolize the symmetry plane. Grayscale: Q^2_{11}. $\theta = 90^\circ$, $L^*_1 = 1$.

larger interfacial distortions. We wish to point out here that instead of tuning the value of L^*_1 in Fig. 3, we could have just as well adjust the value of the anchoring strength W at the Iso-N interface. In fact, it was shown in Ref. [39] that Δy_I is an increasing function of W. Thus, there are two ways of amplifying interfacial deformations: Either increase W while keeping L_1 constant or decrease L_1 at constant W as we did in the present work. Actually, in either case, we decrease the so-called anchoring extrapolation length $L_W = L_1/W$, meaning that the LC molecules are more and more forced to point along the prescribed anchoring direction at the interface. This generates a situation of higher anchoring conflict at the CL and the system responds to that by deforming more the interface and pushing the particle further into the nematic bulk as we showed.

B. P-H configuration

To emphasize the differences with the H-H configuration, we now consider the P-H configuration (cf. Fig. 1) for which there is no anchoring conflict at the CL provided the contact angle is equal to 90°, which is the case here. We employ a similar procedure and the same physical parameters as those used in the H-H setup. As expected, the equilibrium director field differs from that computed in the H-H configuration, and a topological defect of winding number $-1/2$ now forms underneath the particle at a finite distance from its surface as shown in snapshot (a) of Fig. 5. The dark lobes located on either side of the defect signal areas of sizable elastic distortions.

The results of the pair interaction potential are displayed in Fig. 5 for a range of separation distances. As in Fig. 3, the shaded area around the data points represents the uncertainty interval on the total force computation, which amounts to $\pm 1.2 \times 10^{-3}$ here. We see that the interaction potential is exclusively repulsive with a sharp increase of the repulsion at short range. Whatever the separation, and whether we use $L^*_1 = 1$ or $L^*_1 = 0.5$, both the interfacial deformations and particle displacement are extremely small, with typical values $\Delta y_I \approx 0.002R$ and $y_p \approx 0.003R$. This is in stark contrast with the values obtained in the H-H setup, where Δy_I, $y_p \sim 0.4R$ [cf. Fig. 4(a)]. Thus, in the P-H configuration, the interaction potential is completely dominated by elastic effects with a negligible contribution from capillary forces.

Interestingly, an unexpected phenomenon appears at very short range, as illustrated in Fig. 5(b): The defect located below the particle, which is usually aligned with the particle center as in Fig. 5(a), gets a bit shifted towards the other nearby particle. This defect motion only occurs for a small-enough separation distance and is a direct consequence of the symmetry BC prescribed on this plane (Fig. 1). We have checked that it is not correlated to the presence of the other nearby particle for it is indeed well known that topological defects with equal winding numbers repel one another elastically [10,58]. At close range, and with the imposed BCs, we may rather conjecture that the system finds a way of minimizing elastic distortions in the squeezed space between the particle by bringing slightly the defects closer to the symmetry plane.

IV. CONCLUDING REMARKS

In this work, we have carried out numerical simulations on the pair interaction of solid micrometer-sized particles trapped at the Iso-N interface. The particles are subject to elastocapillary interactions driven by both elastic and interfacial deformations. To capture such phenomena, we have used a model that combines a diffuse interface method (PF) to account for the properties of the Iso-N interface with a tensor order parameter description of the nematic phase, including topological defects. Such a model is well suited to describe the coupling between elasticity and capillarity, as shown in previous studies [37–39]. We have primarily focused our attention to the particular situation where there is an anchoring conflict at the CL. Such a conflict can be achieved by prescribing, e.g., a homeotropic anchoring of the LC molecules at both the particle surface and the Iso-N interface. In this configuration, it was demonstrated that significant interfacial deformations and particle displacements, on the order of the particle radius, occur in the vicinity of the floating object [39]. With these anchoring conditions, we have computed the interaction force acting on a pair of particles for several separation distances. Among the salient results, we have found that, although the interaction potential is always repulsive at short range, attractive capillary forces may dominate their repulsive elastic counterparts at intermediate distances, provided the anchoring is strong enough at the Iso-N interface. In this case, the anchoring conflict is enhanced, leading to larger interfacial distortions and attractive capillary forces. However, in the absence of an anchoring conflict at the CL, there is no interfacial deformation nor particle displacement. In this case, the interaction potential is repulsive for all separation distances and dominated by elastic effects.

TABLE I. Definitions and base values of the parameters used in the simulations. The subscript "n" (respectively, "i") denotes nematic (respectively, isotropic). "PF" denotes phase field.

Parameter	Symbol	Value	Unit
Elastic constant	L_1	5–10	pN
Scalar order parameter at equilibrium	q_e	0.81 [38]	—
Nematic rotational viscosity	$\gamma_1 = 1/\Gamma$	0.04	Pa s
Density	ρ_n , ρ_i	10^3	kg m^{-3}
Viscosity	η_n , η_i	0.07	Pa s
Surface tension	σ	2.25×10^{-3}	N m^{-1}
Anchoring strength	W_s	10^{-3}	N m^{-1}
Particle radius	R	1	μm
Contact angle	θ	90°	deg
Capillary width (PF)	ϵ	20	nm
Mobility (PF)	γ	4×10^{-15}	m^2/(Pa s)
Box dimensions (height,length)	(H, L)	$(16R, 28R)$	μm

Overall, our results highlight the importance of having an anchoring conflict at the CL in order to generate sizable interfacial deformations and, thereby, large-enough attractive capillary forces able to compete with their elastic counterparts. Thus, a key finding is that anchoring conflicts appear to be of primary importance to control the self-assembly properties of particles adsorbed at Iso-N interfaces. This prediction brings about new insight on a topic for which there is a dearth of modeling and numerical studies. We hope that the trends derived here in two dimensions hold as well in three dimensions, where a more direct comparison to existing experiments can be made [24,27,32].

In this study, we have only considered a 90° contact angle because it is for this value that the anchoring conflict at the CL is the strongest in the H-H configuration. In this case, we can anticipate that any other θ value will dwindle capillary forces because of smaller interfacial deformations. However, the opposite trend is expected in the P-H configuration for which capillary effects should have a growing influence as θ deviates more and more from 90°. Exploring these new configurations is part of ongoing simulation efforts to complement and strengthen our findings.

So far, most investigations in the field focused on the nematic phase. But, as mentioned in the Introduction, elastocapillary interactions also occur with more ordered LC phases such as smectics in the free-standing film geometry [33]. In such systems, the physical picture is more complex as the meniscus surrounding solid inclusions contains a high density of (edge) dislocations and usually takes the shape of a corona that is often decorated with stripes and/or focal conics domains [59,60]. The detailed structure of smectic mesnici is still not yet fully understood despite recent progress [61]. Understanding the inner workings of elastocapillary interactions in these systems is a challenging and potentially exciting research prospect.

ACKNOWLEDGMENTS

The author thanks M. Qiu, A. Choudhury, and J. J. Feng for enlightening discussions. This work was financially supported by the EU Marie-Curie fellowship "CoPEC" under Grant No. 794837–H2020-MSCA-IF-2017. The author is also indebted to the University of Bordeaux for further financial support thanks to the IdEx program entitled "Développement des carrières–Volet personnel de recherche." The IT staff of the laboratory is gratefully acknowledged for their valuable help and support.

APPENDIX A: SIMULATION PARAMETERS

The parameters characterizing the nematic LC are close to those of the widely used compound 5CB and can be found in Ref. [38]. The numerical parameters for the CH dynamics (capillary width ϵ, mobility γ) are chosen according to the guidelines reported in Refs. [41,44,46]. The dimensional base values of all simulation parameters are listed in the Table I.

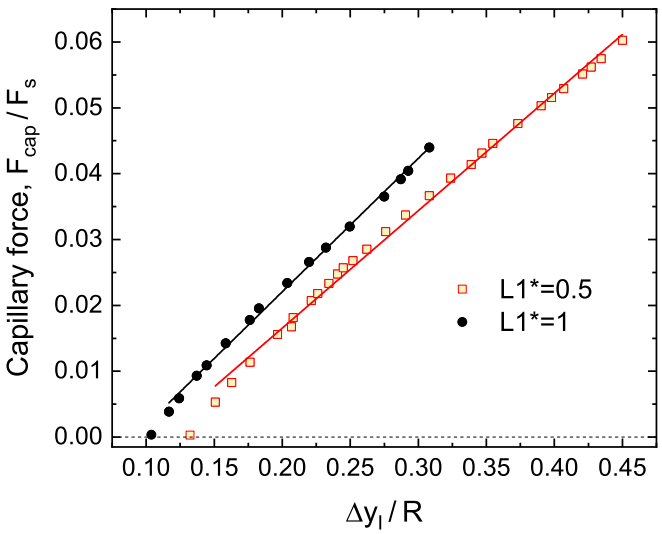

FIG. 6. Proportionality relationship between the capillary interaction force F_{cap} and the interfacial deformation Δy_l for two values of the elastic constant L_1^*.

APPENDIX B: CAPILLARY FORCE VS INTERFACIAL DEFORMATIONS

Figure 6 exhibits the variations of the capillary interaction force $F_{\rm cap}$ as a function of the interfacial deformation Δy_I for the two L_1^* values explored in this work. In both cases, if we discard the first data point corresponding to a very small force, i.e., the particles are far away from each other, then we see that $F_{\rm cap} \propto \Delta y_I$, as shown by the linear fits. Since $\Delta y_I \sim L_1^{-1/2}$, it follows that $F_{\rm cap} \sim L_1^{-1/2}$, as mentioned in the main text and illustrated in the inset of Fig. 4(c).

[1] D. Y. C. Chan, J. D. Henry, Jr., and L. R. White, The interaction of colloidal particles collected at fluid interfaces, J. Colloid Interface Sci. **79**, 410 (1981).

[2] C. Allain and M. Cloitre, Interaction between particles trapped at fluid interfaces, J. Colloid Interface Sci. **157**, 261 (1993).

[3] P. A. Kralchevsky and K. Nagayama, Capillary interactions between particles bound to interfaces, liquid films and biomembranes, Adv. Colloid Interface Sci. **85**, 145 (2000).

[4] M. Oettel and S. Dietrich, Capillary interactions at fluid interfaces, Langmuir **24**, 1425 (2008).

[5] K. D. Danov and P. A. Kralchevsky, Capillary forces between particles at a liquid interface: General theoretical approach and interactions between capillary multipoles, Adv. Colloid Interface Sci. **154**, 91 (2010).

[6] R. McGorty, J. Fung, D. Kaz, and V. N. Manoharan, Colloidal self-assembly at an interface, Mater. Today **13**, 34 (2010).

[7] L. Botto, E. P. Lewandowski, Jr., M. Cavallaro, and K. J. Stebe, Capillary interactions between anisotropic particles, Soft Matter **8**, 9957 (2012).

[8] S. Dasgupta, T. Auth, and G. Gompper, Nano- and microparticles at fluid and biological interfaces, J. Phys.: Condens. Matter **29**, 373003 (2017).

[9] I. B. Liu, N. Sharifi-Mood, and K. J. Stebe, Capillary assembly of colloids: Interactions on planar and curved interfaces, Annu. Rev. Condens. Matter Phys. **9**, 283 (2018).

[10] P. G. de Gennes and J. Prost, *The Physics of Liquid Crystals*, 2nd ed. (Clarendon, Oxford, 1993).

[11] I. I. Smalyukh, Liquid crystal colloids, Annu. Rev. Condens. Matter Phys. **9**, 207 (2018).

[12] P. Poulin, H. Stark, T. C. Lubensky, and D. A. Weitz, Novel colloidal interactions in anisotropic fluids, Science **275**, 1770 (1997).

[13] T. C. Lubensky, D. Pettey, N. Currier, and H. Stark, Topological defects and interactions in nematic emulsions, Phys. Rev. E **57**, 610 (1998).

[14] J.-C. Loudet, P. Barois, P. Auroy, P. Keller, H. Richard, and P. Poulin, Colloidal structures from bulk demixing in liquid crystals, Langmuir **20**, 11336 (2004).

[15] I. Muševič, M. Škarabot, U. Tkalec, M. Ravnik, and S. Žumer, Two-dimensional nematic colloidal crystals self-assembled by topological defects, Science **313**, 954 (2006).

[16] M. Ravnik, M. Škarabot, S. Žumer, U. Tkalec, I. Poberaj, D. Babič, N. Osterman, and I. Muševič, Entangled nematic colloidal dimers and wires, Phys. Rev. Lett. **99**, 247801 (2007).

[17] U. Tkalec, S. Čopar, M. Ravnik, S. Žumer, and I. Muševič, Reconfigurable knots and links in chiral nematic colloids, Science **333**, 62 (2011).

[18] C. Blanc, D. Coursault, and E. Lacaze, Ordering nano- and microparticles assemblies with liquid crystals, Liq. Cryst. Rev. **1**, 83 (2013).

[19] G. Foffano, J. S. Lintuvuori, A. Tiribocchi, and D. Marenduzzo, The dynamics of colloidal inclusions in liquid crystals: a simulation perspective, Liq. Cryst. Rev. **2**, 1 (2014).

[20] D. Abras, G. Pranami, and N. L. Abbott, The mobilities of micro- and nano-particles at interfaces of nematic liquid crystals, Soft Matter **8**, 2026 (2012).

[21] M. A. Gharbi, D. Seč, T. Lopez-Leon, M. Nobili, M. Ravnik, S. Žumer, and C. Blanc, Microparticles confined to a nematic liquid crystal shell, Soft Matter **9**, 6911 (2013).

[22] H. Jeridi, M. A. Gharbi, T. Othman, and C. Blanc, Capillary-induced giant elastic dipoles in thin nematic films, Proc. Natl. Acad. Sci. USA **112**, 14771 (2015).

[23] H. Jeridi, M. Tasinkevych, T. Othman, and C. Blanc, Colloidal particles in thin nematic wetting films, Langmuir **32**, 9097 (2016).

[24] I. I. Smalyukh, S. Chernyshuk, B. I. Lev, A. B. Nych, U. Ognysta, V. G. Nazarenko, and O. D. Lavrentovich, Ordered droplet structures at the liquid crystal surface and elastic-capillary interactions, Phys. Rev. Lett. **93**, 117801 (2004).

[25] A. B. Nych, U. M. Ognysta, V. M. Pergamenshchik, B. I. Lev, V. G. Nazarenko, I. Muševič, M. Škarabot, and O. D. Lavrentovich, Coexistence of two colloidal crystals at the nematic-liquid-crystal-air interface, Phys. Rev. Lett. **98**, 057801 (2007).

[26] T. Yamamoto and M. Yoshida, Self-assembled pseudo-hexagonal structures of colloidal particles at air-liquid crystal interface, Appl. Phys. Express **2**, 101501 (2009).

[27] M. A. Gharbi, M. Nobili, M. In, G. Prévot, P. Galatola, J. B. Fournier, and C. Blanc, Behavior of colloidal particles at a nematic liquid crystal interface, Soft Matter **7**, 1467 (2011).

[28] N. Wang, J. S. Evans, C. Li, V. M. Pergamenshchik, I. I. Smalyukh, and S. He, Controlled multistep self-assembling of colloidal droplets at a nematic liquid Crystal-air interface, Phys. Rev. Lett. **123**, 087801 (2019).

[29] I. H. Lin, Jr., G. M. Koenig, J. J. de Pablo, and N. L. Abbott, Ordering of solid microparticles at liquid crystal-water interfaces, J. Phys. Chem. B **112**, 16552 (2008).

[30] G. M. Koenig, Jr., I. H. Lin, and N. L. Abbott, Chemoresponsive assemblies of microparticles at liquid crystalline interfaces, Proc. Natl. Acad. Sci. USA **107**, 3998 (2010).

[31] I. B. Liu, M. A. Gharbi, V. L. Ngo, R. D. Kamien, S. Yang, and K. J. Stebe, Elastocapillary interactions on nematic films, Proc. Natl. Acad. Sci. USA **112**, 6336 (2015).

[32] W. S. Wei, M. A. Gharbi, M. A. Lohr, T. Still, M. D. Gratale, T. C. Lubensky, K. J. Stebe, and A. G. Yodh, Dynamics of ordered colloidal particle monolayers at nematic liquid crystal interfaces, Soft Matter **12**, 4715 (2016).

[33] M. A. Gharbi, D. A. Beller, N. Sharifi-Mood, R. Gupta, R. D. Kamien, S. Yang, and K. J. Stebe, Elastocapillary driven assem-

bly of particles at free-standing smectic-A films, Langmuir **34**, 2006 (2018).
[34] D. Andrienko, M. Tasinkevych, and S. Dietrich, Effective pair interactions between colloidal particles at a nematic-isotropic interface, Europhys. Lett. **70**, 95 (2005).
[35] M. Tasinkevych and D. Andrienko, Colloidal particles in liquid crystal films and at interfaces, Condens. Matter Phys. **13**, 33603 (2010).
[36] M. Oettel, A. Domínguez, M. Tasinkevych, and S. Dietrich, Effective interactions of colloids on nematic films, Eur. Phys. J. E **28**, 99 (2009).
[37] M. Qiu, Computational studies on interfacial dynamics in complex fluids, Ph.D thesis, University of British Columbia, 2020.
[38] M. Qiu, J. J. Feng, and J.-C. Loudet, Phase-field model for elastocapillary flows of liquid crystals, Phys. Rev. E **103**, 022706 (2021).
[39] J.-C. Loudet, A. Choudhury, M. Qiu, and J. J. Feng, Particle trapped at the isotropic-nematic liquid crystal interface: Elastocapillary phenomena and drag forces, Phys. Rev. E **105**, 044607 (2022).
[40] D. Jacqmin, Calculation of two-phase Navier-Stokes flows using phase-field modeling, J. Comput. Phys. **155**, 96 (1999).
[41] P. Yue, J. J. Feng, C. Liu, and J. Shen, A diffuse-interface method for simulating two-phase flows of complex fluids, J. Fluid Mech. **515**, 293 (2004).
[42] A. N. Beris and B. J. Edwards, *Thermodynamics of Flowing Systems with Internal Microstructure* (Oxford University Press, New York, 1994).
[43] C. Denniston, E. Orlandini, and J. M. Yeomans, Lattice Boltzmann simulations of liquid crystal hydrodynamics, Phys. Rev. E **63**, 056702 (2001).
[44] P. Yue, C. Zhou, J. J. Feng, C. F. Ollivier-Gooch, and H. H. Hu, Phase-field simulations of interfacial dynamics in viscoelastic fluids using finite elements with adaptive meshing, J. Comput. Phys. **219**, 47 (2006).
[45] *COMSOL Multiphysics Reference Manual*, version 6.1, COMSOL, Inc, www.comsol.com.
[46] P. Yue, C. Zhou, and J. J. Feng, Sharp-interface limit of the Cahn-Hilliard model for moving contact lines, J. Fluid Mech. **645**, 279 (2010).
[47] M. Wörner, Numerical modeling of multiphase flows in microfluidics and micro process engineering: a review of methods and applications, Microfluid Nanofluid **12**, 841 (2012).
[48] In our simulations, W has the dimensions of [energy×length]. In the sharp-interface limit, it can be related to the usual anchoring strength, W_s [J/m^2], via $W = \frac{35}{8\sqrt{2}} W_s \epsilon^3$, as explained in Ref. [38].
[49] P. Seppecher, Moving contact lines in the Cahn-Hilliard theory, Int. J. Eng. Sci. **34**, 977 (1996).
[50] D. Jacqmin, Contact-line dynamics of a diffuse fluid interface, J. Fluid Mech. **402**, 57 (2000).
[51] T. Qian, X. P. Wang, and P. Sheng, Molecular hydrodynamics of the moving contact line in two-phase immiscible flows, Commun. Comput. Phys. **1**, 1 (2006).
[52] P. Singh and D. D. Joseph, Fluid dynamics of floating particles, J. Fluid Mech. **530**, 31 (2005).
[53] Note that capillary interactions can be either attractive or repulsive, depending on the type of the overlapping menisci. In our situation [Figs. 2(b) and 2(c)], they are attractive as it is well known that like (respectively, unlike) menisci, e.g., both concave (respectively, e.g., one concave and one convex), attract (respectively, repel) one another (see, e.g., Refs. [3,52]).
[54] F. R. Hung, O. Guzmán, B. T. Gettelfinger, N. L. Abbott, and J. J. de Pablo, Anisotropic nanoparticles immersed in a nematic liquid crystal: Defect structures and potentials of mean force, Phys. Rev. E **74**, 011711 (2006).
[55] R. W. Ruhwandl and E. M. Terenjev, Long-range forces and aggregation of colloid particles in a nematic liquid crystal, Phys. Rev. E **55**, 2958 (1997).
[56] J.-C. Loudet and P. Poulin, Application of an electric field to colloidal particles suspended in a liquid-crystal solvent, Phys. Rev. Lett. **87**, 165503 (2001).
[57] I. I. Smalyukh, O. D. Lavrentovich, A. N. Kuzmin, A. V. Kachynski, and P. N. Prasad, Elasticity-mediated self-organization and colloidal interactions of solid spheres with tangential anchoring in a nematic liquid crystal, Phys. Rev. Lett. **95**, 157801 (2005).
[58] For example, instead of the symmetry BC imposed in the middle of the simulation box, we have used a simple Dirichlet BC where the orientation of LC molecules is prescribed to be parallel to the x axis. In doing so, we are no longer simulating a pair interaction since the other particle is absent. Yet, the same defect motion occurs for close-enough distances from the right wall, thereby ruling out a possible two-particle effect.
[59] K. Harth and R. Stannarius, Corona patterns around inclusions in freely suspended smectic films, Eur. Phys. J. E **28**, 265 (2009).
[60] M. Selmi, J.-C. Loudet, P. V. Dolganov, T. Othman, and P. Cluzeau, Structures in the meniscus of smectic membranes: the role of dislocations? Soft Matter **13**, 3649 (2017).
[61] N. V. Madhusudana, Curvature elasticity of smectic-C liquid crystals and formation of stripe domains along thickness gradients in menisci of free-standing films, Phys. Rev. E **102**, 032701 (2020).